

# Hadronic decay branching ratio measurements of the Higgs boson at future colliders using the Holistic Approach

---

**Jianfeng Jiang**<sup>a,b</sup> **Yongfeng Zhu**<sup>a</sup> **Manqi Ruan**<sup>a,1</sup>

<sup>a</sup>*Institute of High Energy Physics, Chinese Academy of Sciences, Beijing 100049, China*

<sup>b</sup>*University of Chinese Academy of Sciences (UCAS), Beijing 100049, China*

*E-mail:* [manqi.ruan@ihep.ac.cn](mailto:manqi.ruan@ihep.ac.cn)

**ABSTRACT:** Accurately measuring the properties of the Higgs boson is one of the primary physics objectives of the high-energy frontier. Using a holistic approach that incorporates the inclusive information of reconstructed particles, we estimate the relative statistical uncertainty for the Higgs decay modes  $H \rightarrow b\bar{b}$ ,  $c\bar{c}$ ,  $gg$ ,  $WW^*$ , and  $ZZ^*$  at the Circular Electron–Positron Collider (CEPC) operating as a Higgs factory with an integrated luminosity of  $20 \text{ ab}^{-1}$ . In the  $Z(\mu^+\mu^-)H$  and  $Z(\nu\bar{\nu})H$  channels, the relative statistical uncertainties for these decay modes are projected to range from 0.38% to 6.56% and 0.17% to 2.55%, respectively. Notably, the projected precisions for  $H \rightarrow b\bar{b}$ ,  $c\bar{c}$ ,  $gg$ , and  $WW^*$  closely approach the statistical limits, while the  $H \rightarrow ZZ^*$  channel remains approximately a factor of two to four with respect to the statistical limits. Compared to the CEPC Snowmass results, the holistic approach boosts the measurement precision by a factor of two to three. The scaling behavior, specifically the dependence of the anticipated accuracy on the training dataset size, is also observed and analyzed.

---

<sup>1</sup>Corresponding author.

---

## Contents

<b>1</b>	<b>Introduction</b>	<b>1</b>
<b>2</b>	<b>Detector, Samples, and Holistic Approach</b>	<b>2</b>
<b>3</b>	<b>Higgs Hadronic Decay Measurements</b>	<b>4</b>
3.1	$\mu^+\mu^-H$	5
3.2	$\nu\bar{\nu}H$	7
3.3	Combination	9
<b>4</b>	<b>Scaling behavior with Data Size</b>	<b>11</b>
4.1	Signal Efficiencies and Misidentification Rates	11
4.2	Asymptotic Behavior of Anticipated Accuracies	12
4.3	With/Without Pre-Selection	14
4.4	Generator Independence and Robustness	15
<b>5</b>	<b>Discussion and Summary</b>	<b>16</b>
<b>6</b>	<b>Acknowledgements</b>	<b>17</b>

---

## 1 Introduction

After the discovery of the Higgs boson at the Large Hadron Collider (LHC) in 2012 [1, 2], one of the primary objectives of the high-energy physics has been the precise measurement of its properties, in particular its couplings to Standard Model particles. The dominant decay modes of the Higgs boson,  $H \rightarrow b\bar{b}, c\bar{c}, gg, WW^*,$  and  $ZZ^*$ , are of paramount importance. Collectively, these channels not only account for the vast majority of the Higgs width but also provide crucial probes of the Yukawa couplings, gauge boson couplings, and the loop-induced coupling to gluons. Nevertheless, these measurements are intrinsically difficult at the LHC, as the hadronic signatures are often obscured by the complicated collision environment, characterized by significant pile-up events and overwhelming QCD backgrounds. On the other hand, an electron-positron Higgs factory, which has been identified as the highest priority for future collider facilities [3, 4], offers a clean environment that is ideal for measuring these Higgs hadronic decay processes. Prominent proposals include the Circular Electron–Positron Collider (CEPC)[5–8], the Future Circular Collider (FCC-ee)[9], the International Linear Collider (ILC) [10], and the Compact LInear Collider (CLIC) [11].

Artificial intelligence (AI) has significantly advanced data analysis techniques in high-energy physics. Jet origin identification (JOI) [12] classifies jets according to their underlying parton flavor, while one-to-one reconstruction techniques associate detector hits with

individual reconstructed particles to identify their species [13]. More recently, color-singlet identification algorithms have been developed to directly associate final-state particles with their parent bosons [14]. The holistic approach [14], a novel method for signal-background separation, leverages the dimensionality of input information by nearly two orders of magnitude, and has been observed in toy models to enhance the physics reach by roughly a factor of two to six compared to conventional approaches. To improve the Higgs hadronic decay measurement precision and also to understand the performance of the holistic approach under more realistic conditions, we apply this strategy to the  $Z(\mu^+\mu^-)H$  and  $Z(\nu\bar{\nu})H$  channels at the CEPC, focusing on the measurement of the five dominant hadronic Higgs decay processes:  $H \rightarrow b\bar{b}$ ,  $c\bar{c}$ ,  $gg$ ,  $WW^*$ , and  $ZZ^*$ . Compared to the reported results in the CEPC Snowmass study [15], the measurement precision is improved by up to a factor of two to three. In order to better understand the learning behavior and the data dependency of the model, we further analyze the scaling of measurement precision with respect to the training dataset size and assess its robustness against generator-level uncertainties.

This paper is organized as follows: Section 2 introduces the detector model, software framework, AI algorithm, and simulated data samples used in this analysis. Section 3 presents the analyses in the  $Z(\mu^+\mu^-)H$  and  $Z(\nu\bar{\nu})H$  channels and the combined results. Section 4 discusses the observed scaling behavior and the generator robustness of the holistic approach. Section 5 provides a summary and outlook.

## 2 Detector, Samples, and Holistic Approach

This study is based on the CEPC operating as a Higgs factory at a center-of-mass energy of 240 GeV, using the AURORA detector model [13]. AURORA is a particle-flow-oriented detector design evolved from the CEPC Conceptual Design Report (CDR) baseline [6]. It features high-granularity electromagnetic and hadronic calorimeters (ECAL and HCAL), a high-precision tracking system with a low material budget, a high-resolution vertex detector, and a large solenoidal magnet enclosing the calorimeters. In addition, both ECAL and HCAL are assumed to provide a per-cell time resolution of 100 ps. A critical figure of merit for hadronic Higgs measurements is the Boson Mass Resolution (BMR). The AURORA detector is designed to achieve a BMR of 2.75%, as illustrated in the invariant mass distributions in the left panel of Figure 1. Within the AURORA detector concept, near-universal particle identification is achieved, as summarized by the reconstruction confusion matrix in the right panel of Figure 1. The results demonstrate efficiencies of 97%–100% for charged particles and photons, and 75%–80% for neutral hadrons. Fake particles—such as spurious clusters arising from incorrect calorimeter–track associations—are identified with an efficiency of about 77% and a purity of 97.5%.

The samples used in this study are generated with MadGraph\_aMC@NLO[16] and Pythia8[17]. Fast simulations are performed using Delphes [18] for the process  $e^+e^- \rightarrow ZH$  with  $Z \rightarrow \mu^+\mu^-$  or  $\nu\bar{\nu}$ , and with the Higgs boson decaying into the five dominant hadronic modes:  $H \rightarrow b\bar{b}$ ,  $c\bar{c}$ ,  $gg$ ,  $WW^*$ , and  $ZZ^*$ . With this fast simulation, a BMR of approximately 3% is achieved. Standard Model background processes, including  $e^+e^- \rightarrow ZZ$ ,  $WW$ , and  $q\bar{q}$ , are generated to estimate contamination in the signal regions. The cross

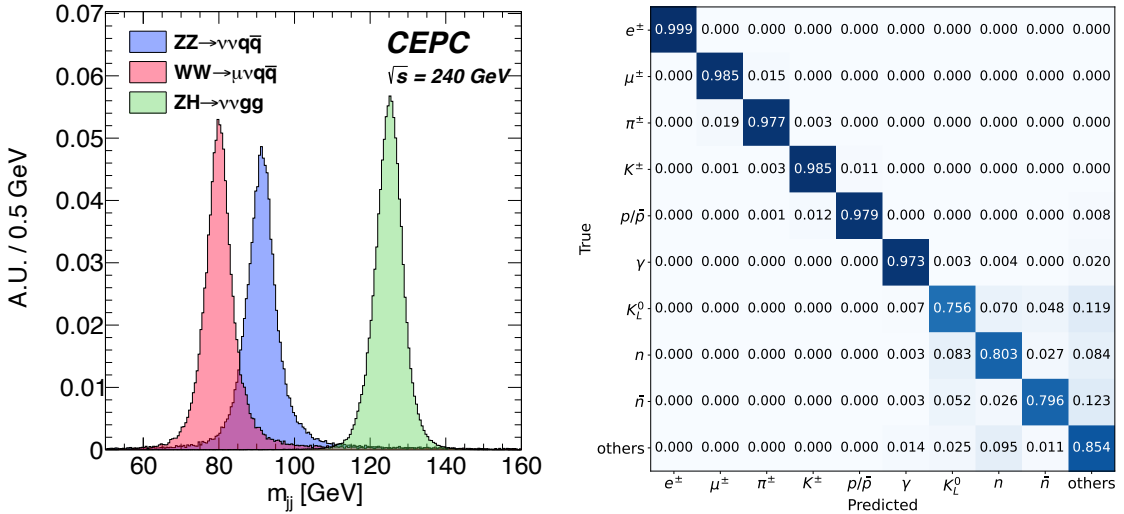


**Figure 1.** Overview of the AURORA detector performance. Left: The reconstructed invariant mass distributions for hadronic systems in  $WW \rightarrow \mu\nu q\bar{q}$ ,  $ZZ \rightarrow \nu\nu q\bar{q}$ , and  $ZH \rightarrow \nu\nu gg$  processes at  $\sqrt{s} = 240$  GeV. Right: Confusion matrix for particle identification (PID) reconstruction, illustrating the identification efficiency for charged particles, photons, and neutral hadrons. The detector concept achieves near-universal particle identification performance.

Channel	Cross section ( $\times$ BR) [fb]	Expected yield ( $20 \text{ ab}^{-1}$ )
$Z(\mu^+\mu^-)H(b\bar{b})$	3.8	$7.7 \times 10^4$
$Z(\mu^+\mu^-)H(c\bar{c})$	0.19	$3.9 \times 10^3$
$Z(\mu^+\mu^-)H(gg)$	0.57	$1.1 \times 10^4$
$Z(\mu^+\mu^-)H(WW^*)$	0.65	$1.3 \times 10^4$
$Z(\mu^+\mu^-)H(ZZ^*)$	0.086	$1.7 \times 10^3$
$Z(\mu^+\mu^-)Z(q\bar{q})$	51	$1.0 \times 10^6$
$Z(\nu\bar{\nu})H(b\bar{b})$	23	$4.5 \times 10^5$
$Z(\nu\bar{\nu})H(c\bar{c})$	1.2	$2.3 \times 10^4$
$Z(\nu\bar{\nu})H(gg)$	3.4	$6.8 \times 10^4$
$Z(\nu\bar{\nu})H(WW^*)$	3.8	$7.7 \times 10^4$
$Z(\nu\bar{\nu})H(ZZ^*)$	0.51	$1.0 \times 10^4$
$W(l\nu)W(q\bar{q})$	1200	$2.4 \times 10^7$
$Z(\nu\bar{\nu})Z(q\bar{q})$	150	$3.0 \times 10^6$
$q\bar{q}$	54000	$1.1 \times 10^{10}$

**Table 1.** Expected yields and cross section( $\times$ BR) for  $Z(\mu^+\mu^-)H$ ,  $Z(\nu\bar{\nu})H$  and main background processes at 240 GeV center-of-mass energy with an integrated luminosity of  $20 \text{ ab}^{-1}$ .

sections and expected event yields for all signal and background processes, normalized to an integrated luminosity of  $20 \text{ ab}^{-1}$ , are summarized in Table 1.

The holistic approach is implemented using the ParticleNet architecture [19], a dynamic graph neural network that represents each collision event as a particle cloud. The core building block of ParticleNet is the EdgeConv operation, which aggregates features from each particle and its  $k$  nearest neighbors in the event. By stacking multiple EdgeConv blocks, the network performs message passing to learn local and global correlations, enabling the extraction of high-level representations directly from the particle cloud. The EdgeConv layers are followed by a channel-wise global average pooling layer and two fully connected layers, with a softmax activation used to produce event-level classification scores. The input features provided to the network encode comprehensive information from reconstructed particles, including:

- *Geometric coordinates*: The angular variables  $\Delta\eta$  and  $\Delta\phi$ , defined relative to a reference axis.<sup>1</sup>
- *Kinematic variables*: The transverse momentum ( $p_T$ ) and energy ( $E$ ), together with their normalized fractions ( $p_T/p_{T,\text{evt}}$  and  $E/E_{\text{evt}}$ ). The angular distance  $\Delta R = \sqrt{\Delta\eta^2 + \Delta\phi^2}$  and the particle charge are also included.
- *Impact parameters*: The transverse ( $d_0$ ) and longitudinal ( $d_z$ ) impact parameters of the track, which are essential for resolving displaced vertices from heavy-flavor ( $b$  and  $c$ ) decays.
- *Particle identification*: One-hot encoded labels for the seven reconstructed particle species:  $\mu^\pm, e^\pm, \gamma, \pi^\pm, K^\pm, p^\pm$ , and neutral hadrons.

To study the scaling behavior with respect to the size of the training dataset, independent training samples are generated with sizes logarithmically spaced between  $10^4$  and  $10^6$  events. A fixed validation dataset of  $2 \times 10^5$  events is used for hyperparameter tuning and model checkpointing to mitigate overfitting. The final performance, quantified in terms of efficiency, purity, and confusion matrices, is evaluated using an independent inference dataset of  $8 \times 10^5$  events, ensuring statistical robustness.

### 3 Higgs Hadronic Decay Measurements

For the measurement of different Higgs decay processes in  $\mu^+\mu^-H$  and  $\nu\bar{\nu}H$  channels, we use the relative statistical uncertainty to evaluate the measurement performance. The relative statistical uncertainty is calculated as  $\Delta\mu/\mu = \sqrt{S+B}/S$ , where  $S$  and  $B$  denote the expected signal and background yields surviving the selection, respectively.

	$Hb\bar{b}$	$Hc\bar{c}$	$Hgg$	$HWW^*$	$HZZ^*$	$ZZ_{sl}$
$Hb\bar{b}$	93.36%	1.14%	1.00%	0.09%	4.31%	0.10%
$Hc\bar{c}$	0.94%	90.03%	2.68%	3.38%	2.88%	0.10%
$Hgg$	1.89%	2.79%	84.40%	5.93%	4.94%	0.05%
$HWW^*$	0.06%	2.04%	5.82%	82.15%	9.87%	0.05%
$HZZ^*$	3.67%	2.95%	6.26%	18.73%	68.32%	0.07%
$ZZ_{sl}$	0.23%	0.21%	0.17%	0.06%	0.08%	99.25%

**Figure 2.** Confusion matrix for the  $Z(\mu^+\mu^-)H$  classification task using the holistic approach, trained on 1M events. Matrix elements are normalized to a unit in each row.

### 3.1 $\mu^+\mu^-H$

In the  $Z(\mu^+\mu^-)H$  channel, the presence of two isolated high-momentum muons provides an efficient trigger and allows for strong suppression of Standard Model backgrounds, except semileptonic  $ZZ$  production [20]. We therefore apply the holistic approach to directly discriminate among the different Higgs decay processes and the semileptonic  $ZZ$  background. A training dataset of  $10^6$  events are used for each Higgs decay process and for the  $ZZ$  background in a multi-class classification setup.

Figure 2 shows the resulting confusion matrix, where each row represents the classification efficiency for a given process. A pronounced diagonal structure is observed, in which the dominant Standard Model background,  $Z(\mu^+\mu^-)Z(q\bar{q})$ , is strongly suppressed, achieving a classification efficiency of 99.25%. Among the Higgs decay processes,  $H \rightarrow b\bar{b}$  attains the highest classification efficiency. This is primarily due to the presence of multiple secondary vertices in  $b$ -jets and the more compact event topology compared to the broader topologies of  $H \rightarrow WW^*$  and  $H \rightarrow ZZ^*$  decays. The classification efficiencies for  $H \rightarrow c\bar{c}$  and  $H \rightarrow gg$  are 90.03% and 84.40%, respectively. The separation of  $H \rightarrow WW^*$  and  $H \rightarrow ZZ^*$  remains more challenging because of their similar decay topologies, and

<sup>1</sup>To explicitly capture the global topology of the  $ZH$  process, a reference axis is introduced for coordinate transformation. For the  $Z(\mu^+\mu^-)H$  channel, the reference axis is defined by the recoil system (the Higgs candidate),  $p_{\text{recoil}} = p_{\text{initial}} - p_{\mu\mu}$ . For the  $Z(\nu\bar{\nu})H$  channel, it is defined by the missing momentum vector (the  $Z$  boson candidate),  $p_{\text{missing}} = p_{\text{initial}} - p_{\text{visible}}$ . These coordinates are used to construct the dynamic  $k$ -nearest-neighbor graph.

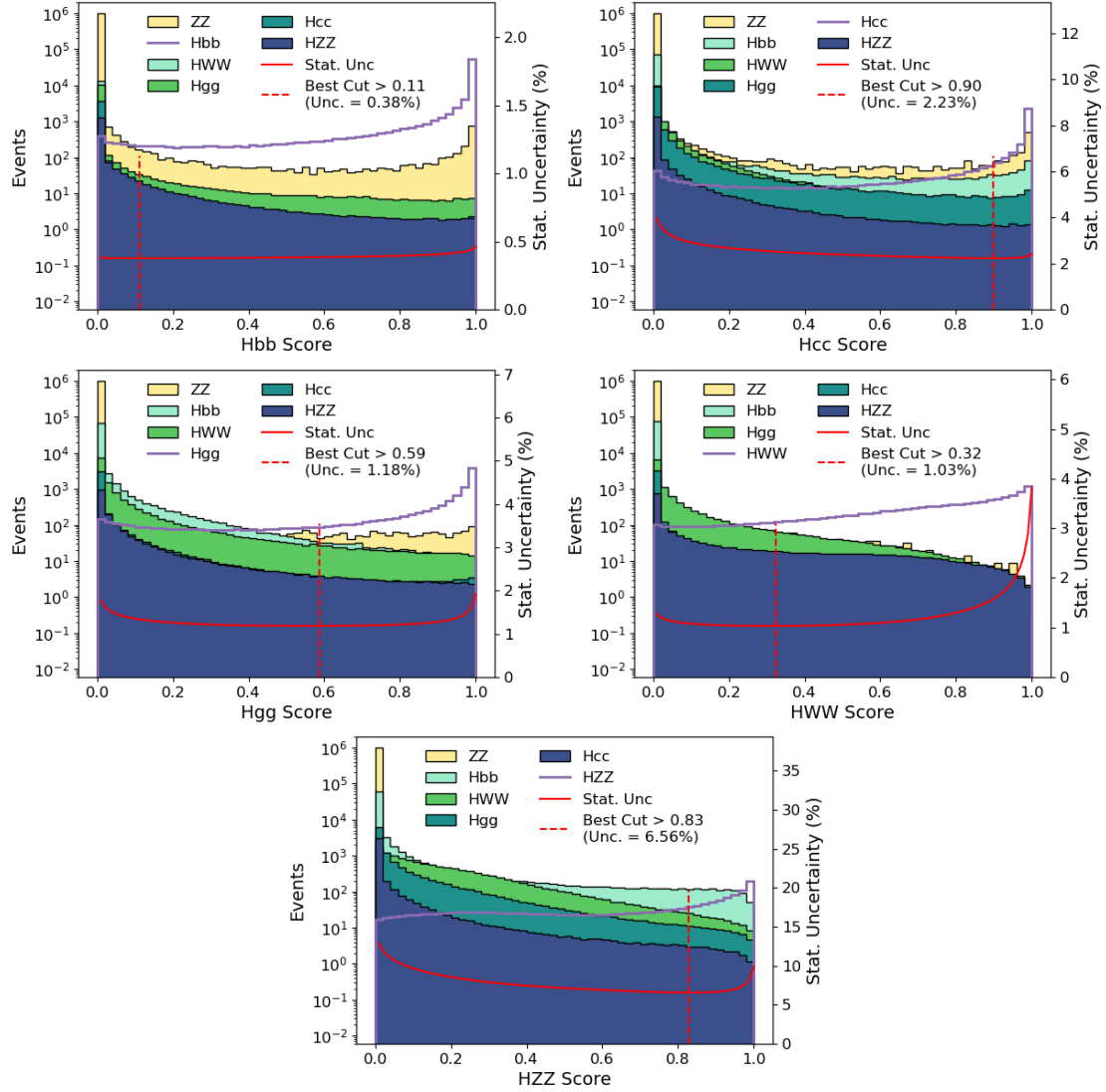


**Figure 3.** Score distributions and relative statistical uncertainties for  $H \rightarrow b\bar{b}$ ,  $H \rightarrow c\bar{c}$ ,  $H \rightarrow gg$ ,  $H \rightarrow WW^*$ , and  $H \rightarrow ZZ^*$  processes in the  $Z(\mu^+\mu^-)H$  analysis using holistic approach trained on 1M events. The purple curve denotes the signal, while the colored histograms show the backgrounds. The red solid curve gives the statistical uncertainty versus the score cut, and the vertical red dashed line marks the optimal score cut.

the observed asymmetric misidentification between these two channels warrants further investigation.

Figure 3 presents the classifier score distributions for  $H \rightarrow b\bar{b}$ ,  $H \rightarrow c\bar{c}$ ,  $H \rightarrow gg$ ,  $H \rightarrow WW^*$ , and  $H \rightarrow ZZ^*$  processes. For the  $H \rightarrow b\bar{b}$  process, characterized by distinct signatures and a relatively large cross-section, a loose selection threshold (score  $> 0.11$ ) is sufficient to achieve high precision. In contrast, the  $H \rightarrow c\bar{c}$  process demands a stringent threshold (score  $> 0.90$ ) to effectively suppress the significant gluon backgrounds. The optimized statistical uncertainties are 0.38% for  $H \rightarrow b\bar{b}$ , 2.23% for  $H \rightarrow c\bar{c}$ , 1.18% for

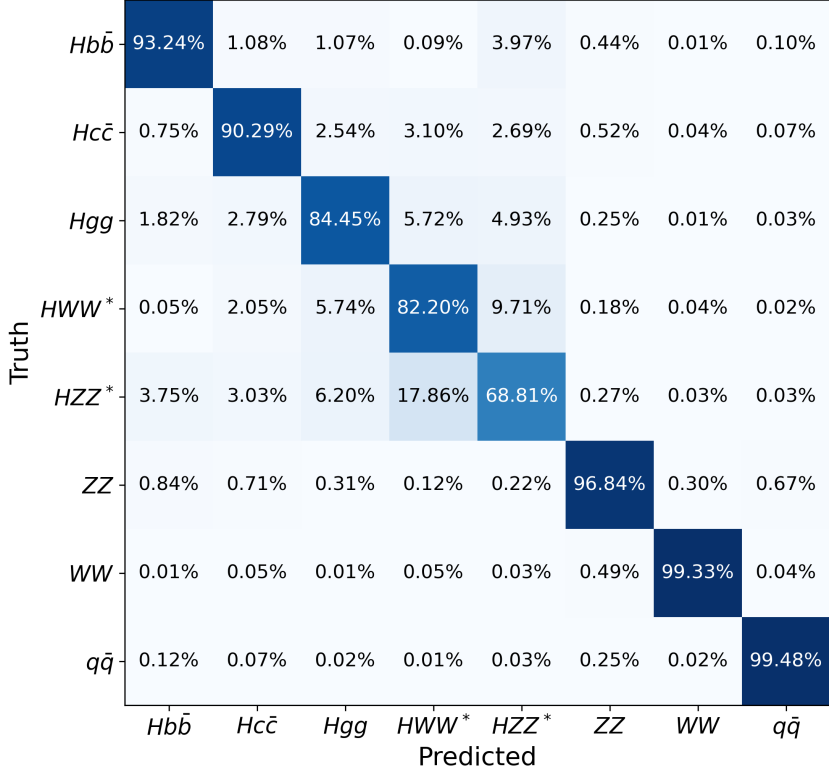


**Figure 4.** Confusion matrix in the  $Z(\nu\bar{\nu})H$  channel using the holistic approach, trained on 1M events. Matrix elements are normalized to a unit in each row.

$H \rightarrow gg$ , 1.03% for  $H \rightarrow WW^*$ , and 6.56% for  $H \rightarrow ZZ^*$ . Notably, except for the  $H \rightarrow ZZ^*$  process, these projections closely approach the ultimate statistical limit ( $1/\sqrt{N_{sig}}$ ) of 0.36%, 1.61%, 0.94%, and 0.88% for  $H \rightarrow b\bar{b}$ ,  $H \rightarrow c\bar{c}$ ,  $H \rightarrow gg$ , and  $H \rightarrow WW^*$ , respectively.

### 3.2 $\nu\bar{\nu}H$

For the  $Z(\nu\bar{\nu})H$  channel, the dominant background contributions arise from four-fermion processes (such as  $e^+e^- \rightarrow ZZ$  and  $e^+e^- \rightarrow W^+W^-$ ) and two-fermion ( $e^+e^- \rightarrow q\bar{q}$ ) processes according to the studies in [21]. Therefore, a pre-selection based on kinematic variables is needed to suppress these backgrounds. These pre-selection criteria are optimized to maximize the product of signal efficiency and signal purity, including:  $p_{T,\text{evt}} > 10$  GeV,  $60 < M_{\text{miss}} < 140$  GeV, and  $105 < M_{\text{inv}} < 160$  GeV, where  $p_{T,\text{evt}}$  is the event transverse momentum,  $M_{\text{miss}}$  is the missing mass calculated from the missing energy and momentum, and  $M_{\text{inv}}$  is the invariant mass of all visible particles. The cut chain is summarized in Table 2.

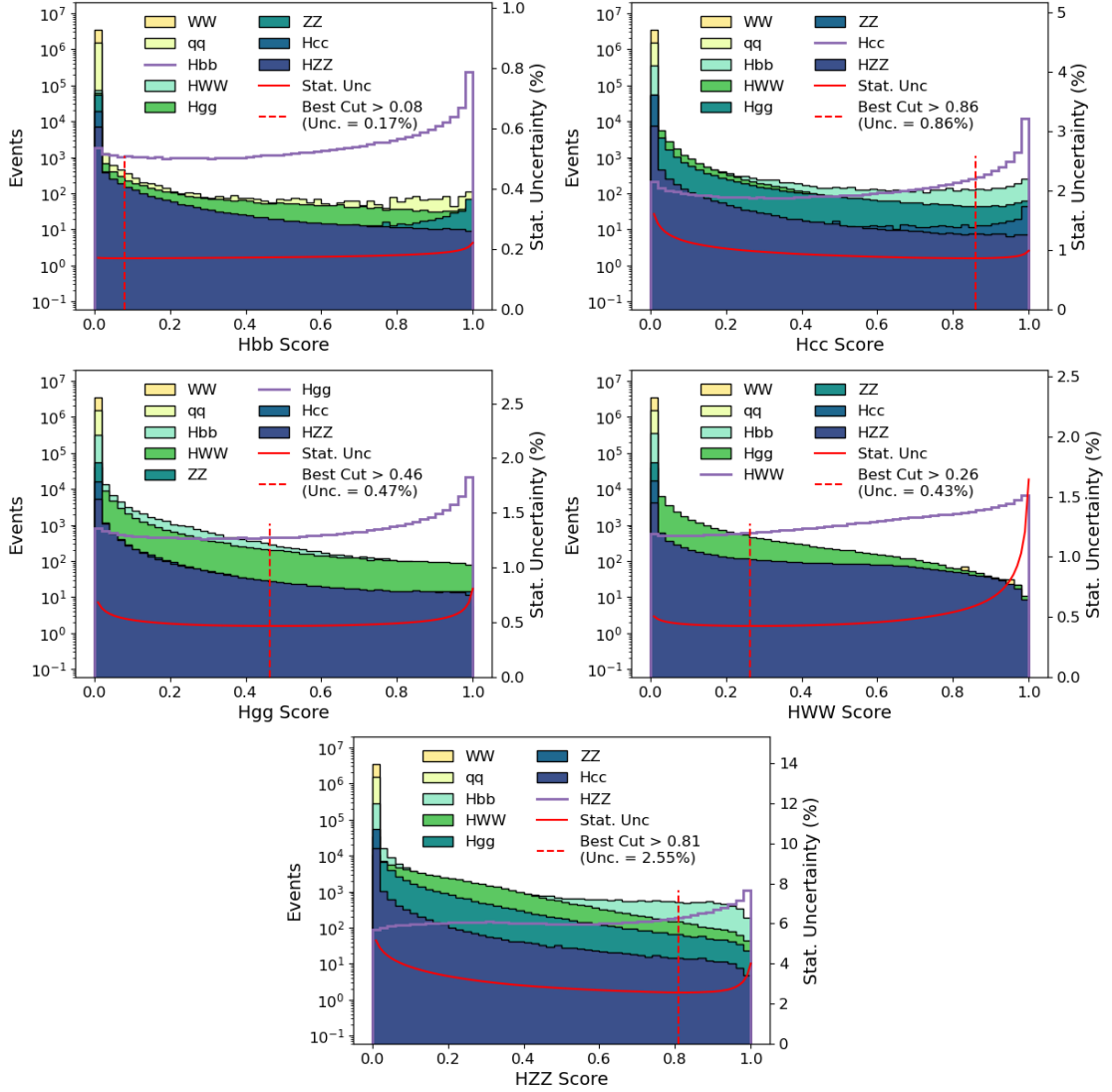


**Figure 5.** Score distributions and relative statistical uncertainties for  $H \rightarrow b\bar{b}$ ,  $H \rightarrow c\bar{c}$ ,  $H \rightarrow gg$ ,  $H \rightarrow WW^*$ , and  $H \rightarrow ZZ^*$  processes in the  $Z(\nu\bar{\nu})H$  analysis using holistic approach trained on 1M events. The purple curve denotes the signal, while the colored histograms show the backgrounds. The red solid curve gives the statistical uncertainty versus the score cut, and the vertical red dashed line marks the optimal score cut.

Following the pre-selection, we employ the same method as used in the  $\mu^+\mu^-H$  channel, where the holistic approach is used to classify different processes. Figure 4 shows the confusion matrix for the classification task. The diagonal elements reflect high classification efficiencies, with 92.57% for  $H \rightarrow b\bar{b}$  and 89.69% for the  $H \rightarrow c\bar{c}$  channel. The dominant Standard Model background  $e^+e^- \rightarrow Z(\nu\bar{\nu})Z(q\bar{q})$  is suppressed with a rejection rate of over 99.42%. The confusion between  $H \rightarrow WW^*$  and  $H \rightarrow ZZ^*$  remains the primary challenge, where 18.90% of  $H \rightarrow ZZ^*$  events are misclassified as  $H \rightarrow WW^*$ .

Figure 5 presents the score distributions for the five Higgs decay processes. By optimiz-

Channel	$p_{T,evt} > 10$ GeV	$60 < M_{miss} < 140$	$105 < M_{inv} < 160$	Eff (%)
$Z(\nu\bar{\nu})H(b\bar{b})$	$4.42 \times 10^5$	$4.29 \times 10^5$	$3.64 \times 10^5$	80.20
$Z(\nu\bar{\nu})H(c\bar{c})$	$2.23 \times 10^4$	$2.20 \times 10^4$	$2.04 \times 10^4$	89.29
$Z(\nu\bar{\nu})H(gg)$	$6.60 \times 10^4$	$6.56 \times 10^4$	$6.43 \times 10^4$	95.30
$Z(\nu\bar{\nu})H(WW^*)$	$7.52 \times 10^4$	$7.48 \times 10^4$	$7.32 \times 10^4$	95.08
$Z(\nu\bar{\nu})H(ZZ^*)$	$9.92 \times 10^3$	$9.84 \times 10^3$	$9.36 \times 10^3$	92.09
$W(l\nu)W(q\bar{q})$	$2.33 \times 10^7$	$5.41 \times 10^6$	$3.45 \times 10^6$	14.12
$Z(\nu\bar{\nu})Z(q\bar{q})$	$2.94 \times 10^6$	$2.78 \times 10^6$	$5.55 \times 10^4$	1.83
$q\bar{q}$	$5.99 \times 10^8$	$4.22 \times 10^8$	$1.51 \times 10^7$	0.14

**Table 2.** The cut flow for  $Z(\nu\bar{\nu})H$  selection and main backgrounds normalized to the integrated luminosity of  $20\text{ ab}^{-1}$  at 240 GeV. The pre-selection requires  $p_{T,evt} > 10$  GeV,  $60 < M_{miss} < 140$  GeV, and  $105 < M_{inv} < 160$  GeV. Here,  $M_{miss}$  is the missing mass calculated from the missing energy and momentum, and  $M_{inv}$  is the invariant mass of all visible particles. The last column shows the overall efficiency after applying the pre-selection.

ing the thresholds on these discriminant scores, we extract the signal events and evaluate the measurement precision. The resulting statistical uncertainties are 0.17% for  $b\bar{b}$ , 0.86% for  $c\bar{c}$ , 0.47% for  $gg$ , 0.43% for  $WW^*$ , and 2.55% for  $ZZ^*$ .

### 3.3 Combination

We evaluate the measurement precision for different Higgs hadronic decay processes in the  $Z(\mu^+\mu^-)H$  and  $Z(\nu\bar{\nu})H$  channels. Figure 6 compares these results with the projections from the CEPC Snowmass study [15] and recent FCC-ee estimates [22]. For the  $H \rightarrow b\bar{b}$ ,  $c\bar{c}$ , and  $gg$  processes, the holistic approach yields significant improvements, reducing the relative uncertainties by a factor of approximately 2 to 3 compared to the Snowmass results. Remarkably, the precisions for these processes, together with  $H \rightarrow WW^*$ , have nearly reached the theoretical statistical limit. On the other hand, the  $H \rightarrow ZZ^*$  process still exhibits a noticeable gap from its statistical limit, indicating that there remains considerable room for further optimization in this complex topology. It should be noted that the current analysis for the  $\nu\bar{\nu}H$  channel focuses exclusively on the Higgs-strahlung process. The  $WW$  fusion, which yields an identical final state, has not been included in this study. At a center-of-mass energy of 240 GeV, the inclusion of the  $WW$ -fusion contribution would effectively increase the signal yield, potentially improving the measurement precision by approximately 5%.

To estimate the full physics potential of future Higgs factories, we extend these rigorous simulation results to the remaining production channels, with the global combination summarized in Table 3. For the high-statistics  $e^+e^- \rightarrow Z(q\bar{q})H$  channel, we assume a sensitivity comparable to that of the  $e^+e^- \rightarrow Z(\nu\bar{\nu})H$  channel, given their similar detector coverage and the capability to fully reconstruct hadronic final states. For the leptonic  $e^+e^- \rightarrow Z(e^+e^-)H$  and  $e^+e^- \rightarrow Z(\tau^+\tau^-)H$  channels, we derive projections from the  $e^+e^- \rightarrow Z(\mu^+\mu^-)H$  baseline by applying a conservative cumulative performance degradation factor of 0.9 (i.e.,  $\delta_{ee} \approx \delta_{\mu\mu}/0.9$  and  $\delta_{\tau\tau} \approx \delta_{ee}/0.9$ ) to account for the relative

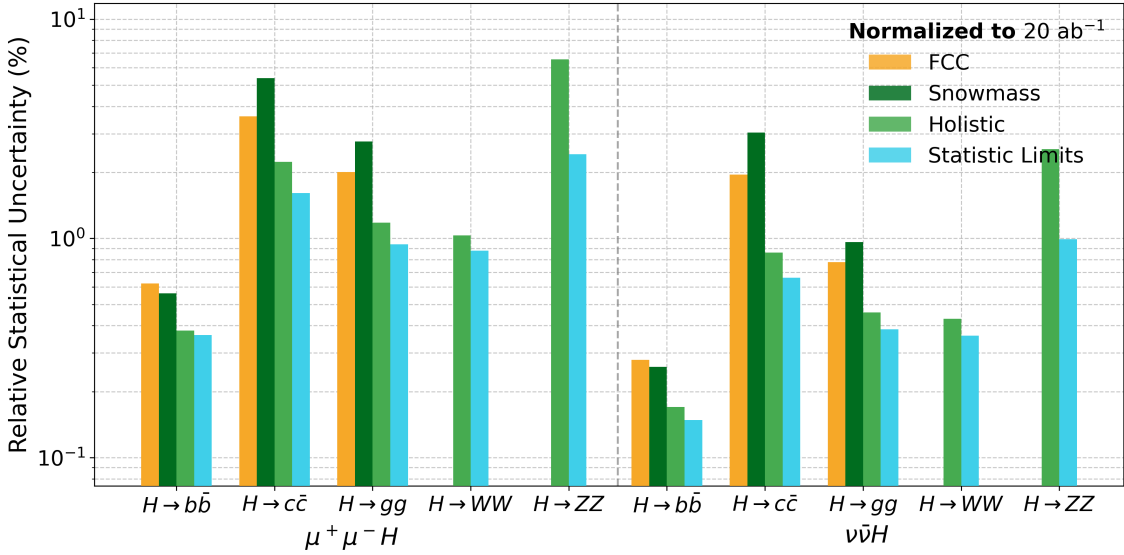


**Figure 6.** Combined precision for each Higgs hadronic decay process using the  $\mu^+\mu^-H$  and  $\nu\bar{\nu}H$  channels. The results obtained via the holistic approach are compared with the CEPC baseline results submitted to Snowmass 2021 (labeled 'Snowmass') [15] and the recent FCC-ee estimates [22]. Since the Snowmass report presents globally combined results, the specific precisions for the reference channels are taken from the individual input studies:  $H \rightarrow b\bar{b}/c\bar{c}/gg$  from [23]

	$H \rightarrow b\bar{b}$	$H \rightarrow c\bar{c}$	$H \rightarrow gg$	$H \rightarrow WW^*$	$H \rightarrow ZZ^*$
$Z(\mu^+\mu^-)H$	0.38%	2.23%	1.18%	1.03%	6.56%
$Z(\nu\bar{\nu})H$	0.17%	0.86%	0.47%	0.43%	2.55%
<b>Combined*</b>	<b>0.11%</b>	<b>0.56%</b>	<b>0.30%</b>	<b>0.28%</b>	<b>1.66%</b>

**Table 3.** Projected relative statistical precision for different Higgs hadronic decay processes across different  $ZH$  decay channels with the integrated luminosity of  $20 \text{ ab}^{-1}$ . The results for  $Z(\mu^+\mu^-)H$  and  $Z(\nu\bar{\nu})H$  are derived from the holistic analysis presented in this work. The combined\* precision incorporates these results along with estimates for the omitted  $Z(q\bar{q})H$ ,  $Z(e^+e^-)H$ , and  $Z(\tau^+\tau^-)H$  channels. The estimation assumes  $Z(q\bar{q})H$  achieves comparable precision to  $Z(\nu\bar{\nu})H$ , while electron and tau channels are projected from the muon channel assuming cumulative performance degradation factors of 0.9 (i.e.,  $\delta_{ee} \approx \delta_{\mu\mu}/0.9$  and  $\delta_{\tau\tau} \approx \delta_{ee}/0.9$ ).

challenges in electron energy resolution and tau reconstruction efficiency compared to the  $e^+e^- \rightarrow Z(\mu^+\mu^-)H$  channel.

These results account only for the statistical uncertainties, while the control of systematic and theoretical uncertainties is critical. In general, the systematic uncertainties of those Higgs measurements could, in principle, be controlled by the  $Z$  boson measurements, given the fact that CEPC could produce six orders of magnitude more  $Z$  bosons compared to the Higgs boson. The relevant systematics on detector performance (acceptance, efficiencies, differential resolution, and identification power) could, in principle, be controlled. Meanwhile, the 1-1 correspondence approach [13] also provides a mechanism

to better monitor and calibrate the detector. It should be remarked that, as the holistic approach significantly improves the anticipated accuracies, the control of relevant systematic uncertainty becomes more challenging. For instance, as the  $H \rightarrow b\bar{b}$  reaches per-mille level accuracy, the systematic uncertainty on luminosity measurements becomes comparable to the statistical error. Thus, the previous target of  $10^{-3}$  for luminosity needs to be further improved. Another key component of the systematic uncertainty involves the calibration and robustness of the method itself, which is partly addressed by analyzing the scaling behavior and generator dependence in Section 4. While a comprehensive evaluation of systematic effects is beyond the scope of this study, we acknowledge that achieving the ultimate experimental precision will critically depend on the rigorous control of these systematics in future analyses.

## 4 Scaling behavior with Data Size

To optimize simulation strategies for future colliders, it is essential to characterize how deep learning performance evolves with available training statistics. While traditional cut-based analyses typically reach a performance plateau at moderate sample sizes, high-dimensional models like ParticleNet theoretically possess the capacity to extract increasingly subtle kinematic correlations from larger datasets. However, the extent to which this capacity translates into measurement precision, and whether it eventually encounters an intrinsic physical limit, remains to be empirically quantified. In this section, we systematically evaluate these learning dynamics. Section 4.1 analyzes the evolution of signal efficiencies and misidentification rates. Section 4.2 models the asymptotic behavior of the anticipated measurement precision. Section 4.3 investigates the influence of physics-driven pre-selection on the learning trajectory. Section 4.4 assesses the model’s robustness against hadronization modeling uncertainties.

### 4.1 Signal Efficiencies and Misidentification Rates

We evaluate the fundamental classification capability of the model as a function of training statistics, varying the dataset size from  $10^4$  to  $10^6$  events. Figure 7 illustrates the evolution of overall accuracy, signal efficiencies, and specific misidentification rates for the  $\mu^+\mu^-H$  channel.

The top-left panel of Figure 7 shows a continuous improvement in the global performance, with the overall accuracy rising from approximately 76% to 86% as the dataset size increases. The signal efficiency curves (top-right panel) demonstrate distinct scaling behaviors across different Higgs decay processes. The vector boson decays ( $H \rightarrow WW^*$ ,  $H \rightarrow ZZ^*$ ) exhibit the steepest improvement slopes, indicating that larger datasets are particularly effective for identifying these four-jet topologies. In parallel, the heavy flavor modes ( $H \rightarrow b\bar{b}$ ,  $H \rightarrow c\bar{c}$ ) show a steady and consistent improvement, with the  $H \rightarrow c\bar{c}$  accuracy increasing by approximately 10~15% without early saturation. Conversely, the  $H \rightarrow gg$  channel displays a comparatively moderate improvement slope relative to the vector boson processes. These trends are consistent with the evolution of specific misidentification rates. As shown in the bottom-right panel, the misidentification of  $H \rightarrow WW^*$  events as  $H \rightarrow b\bar{b}$

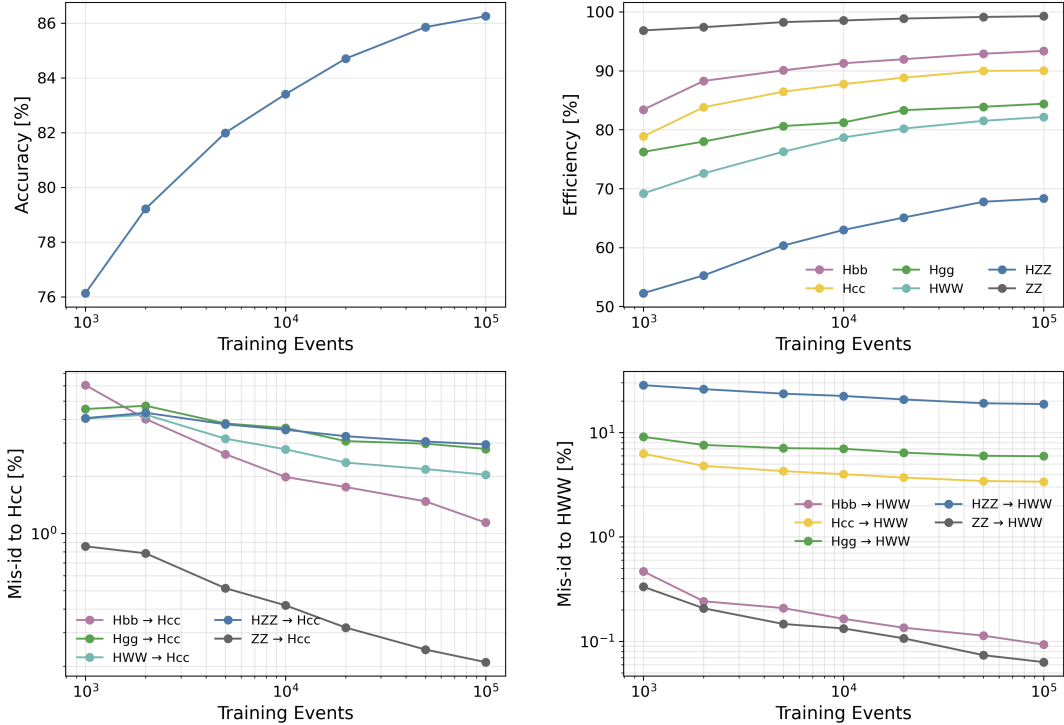


**Figure 7.** Top left: Overall accuracy as a function of training dataset size for the  $Z(\mu^+\mu^-)H$  channels. Top right: Signal efficiency for each decay process versus training dataset size for the  $Z(\mu^+\mu^-)H$  channel. Bottom left: Misidentification rate of  $H \rightarrow c\bar{c}$  versus training dataset size. Bottom right: Misidentification rate of  $H \rightarrow WW^*$  versus training dataset size.

or  $H \rightarrow ZZ^*$  drops precipitously as the dataset expands. In contrast, the misidentification rates for the  $H \rightarrow c\bar{c}$  channel (bottom-left panel) decrease more gradually, remaining the dominant source of background for the  $c\bar{c}$  channel even at the highest statistics point.

## 4.2 Asymptotic Behavior of Anticipated Accuracies

Building on the classification performance, we model the dependence of the physics measurement uncertainty ( $\delta\mu/\mu$ ) on the training dataset size. We employ a power-law ansatz with an irreducible term:

$$y = aN^{-\alpha} + c \quad (4.1)$$

Here,  $\alpha$  denotes the scaling exponent governing the improvement rate, and  $c$  represents the asymptotic uncertainty floor, which corresponds to the irreducible confusion arising from the kinematic overlap between the signal and background phase spaces. Applying this scaling model to the  $Z(\mu^+\mu^-)H$  channel, as shown in Figure 8, the precision improves rapidly with increasing statistics.

A marked divergence in asymptotic behavior is observed between different decay processes. For topologically distinct processes like  $H \rightarrow b\bar{b}$ , the projected precision asymptotically approaches the statistical limit. In the unlimited data regime, the gap between the fitted asymptote  $c$  and the statistical limit becomes negligible, indicating that the network

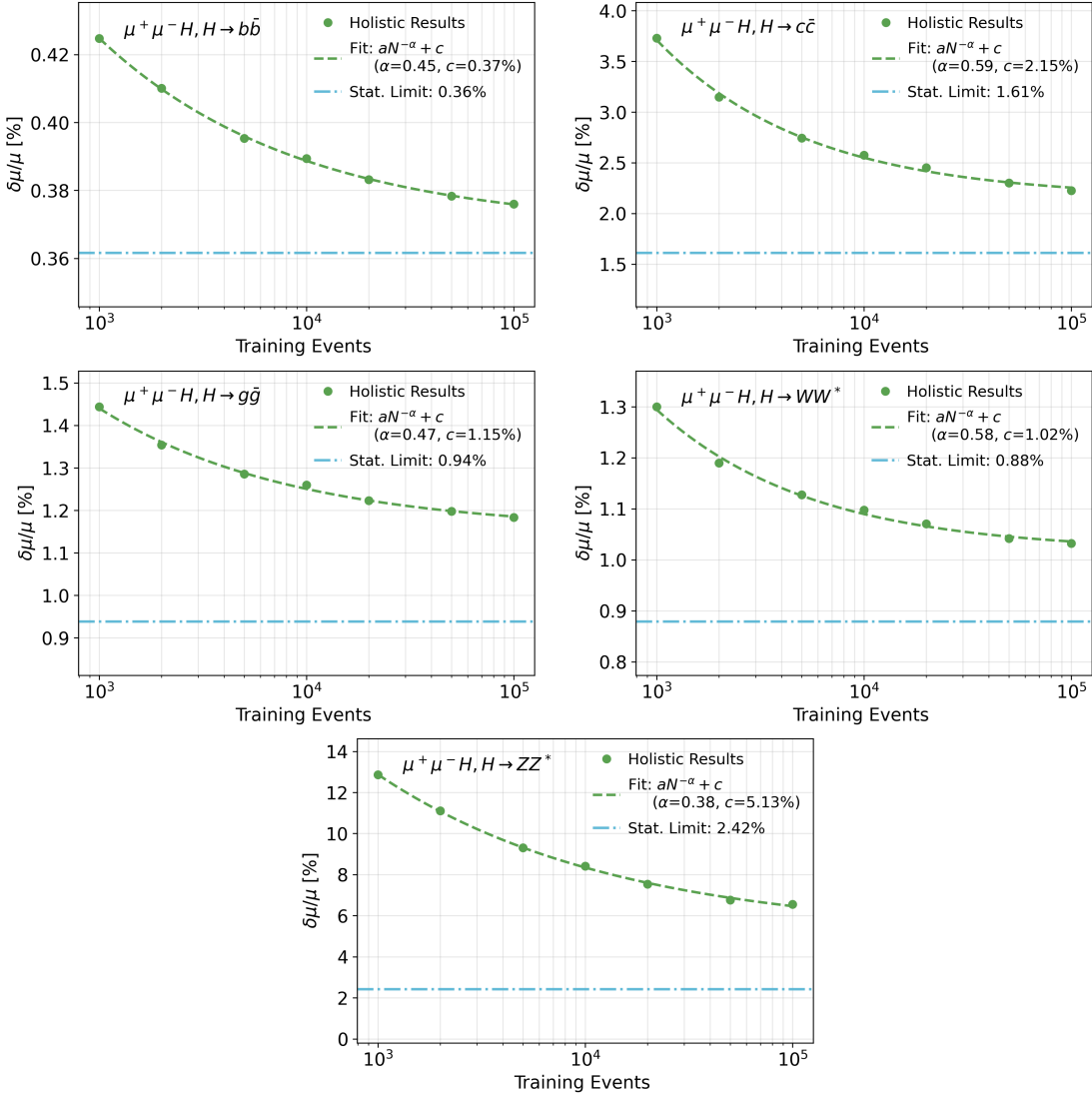


**Figure 8.** Scaling of measurement statistical uncertainty with training dataset size for the  $Z(\mu^+\mu^-)H$  channel.

successfully captured nearly all available discriminating information, achieving an effective identification efficiency close to unity with negligible contamination. Conversely, for complex processes like  $H \rightarrow ZZ^*$ , a noticeable residual gap remains even at high statistics. This indicates the irreducible physical confusion between the kinematically overlapping  $H \rightarrow ZZ^*$  and  $H \rightarrow WW^*$  processes. While increasing training data sharpens the decision boundaries, the presence of this intrinsic ambiguity effectively reduces the statistical significance of the signal, preventing the measurement from fully reaching the purely statistical bound derived from signal counts alone.

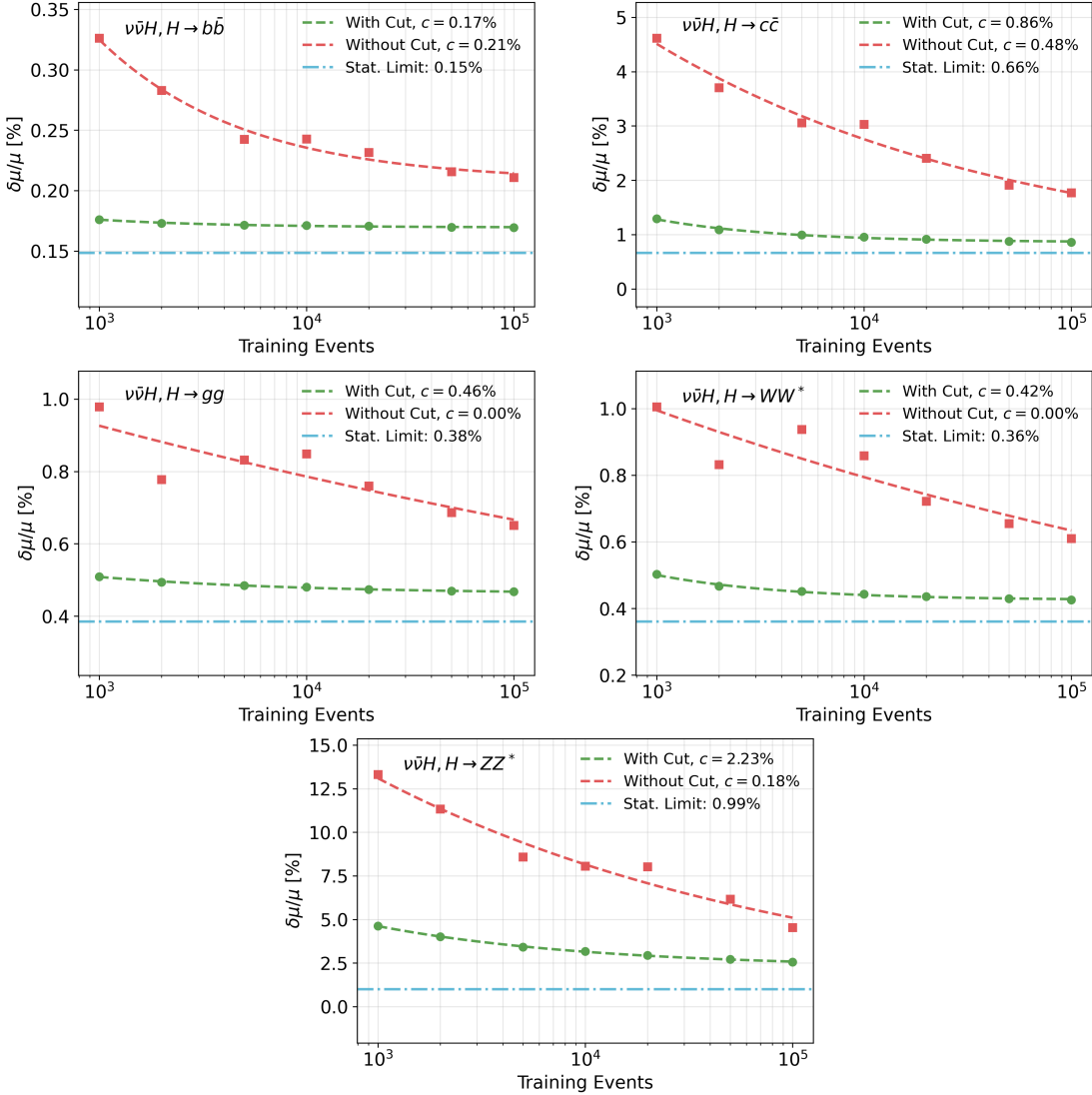


**Figure 9.** Scaling of measurement statistical uncertainty with training dataset size for the  $Z(\nu\bar{\nu})H$  channel, comparing results with and without pre-selection.

### 4.3 With/Without Pre-Selection

In the  $Z(\nu\bar{\nu})H$  channel, we investigate the impact of physical pre-selection on the model’s scaling behavior. Figure 9 compares the holistic approach with and without pre-selection strategy.

The comparison reveals two distinct learning patterns. As shown in the low-statistics region of Figure 9, the pre-selection case converges much faster. This is because the manual cuts remove the vast majority of background events beforehand, effectively telling the network where to focus. Consequently, the learning curve for the pre-selection strategy is relatively flat, indicating the model quickly learns the remaining information but hits a bottleneck. In contrast, the holistic approach (without cuts) starts with higher uncertainties but exhibits a much steeper downward slope. This indicates that while the network

needs more data to resolve the kinematic boundaries on its own, it eventually learns to extract information more efficiently than the hard cuts allow.

Fitting these curves gives us insight into the ultimate potential of each method. For the  $H \rightarrow b\bar{b}$  mode, the cuts are currently very effective. However, for other modes, the fitting parameters suggest a potential crossover: the holistic approach has a lower statistics limit, meaning it could surpass the cut-based method if given enough data.

In such environments ( $B \gg S$ ), applying pre-selection remains a necessary and pragmatic step to stabilize the training and ensure reasonable performance with limited resources. However, our scaling analysis points to a clear future direction: as classification algorithms improve and simulation datasets grow larger, we should aim to remove these artificial truncations. To achieve the ultimate precision limit of the experiment, preserving the full phase space, and allowing the AI to exploit the subtle correlations that human-designed cuts might discard, will be the optimal strategy.

#### 4.4 Generator Independence and Robustness

Dependencies on specific simulation models constitute a major source of systematic uncertainty in ML-based analyses. To evaluate the robustness of our holistic approach against hadronization modeling variations, we perform a cross-validation using Herwig7 [24], which utilizes the Cluster fragmentation model [25], in contrast to the Lund String model [26, 27] used by our training generator, Pythia8. We apply the models trained on Pythia8 datasets of varying sizes to an independent testing dataset generated with Herwig7.

Figure 10 presents the scaling of measurement precision for both generators. The results show two distinct behaviors depending on the decay topology. For the two-body hadronic decays ( $H \rightarrow b\bar{b}, H \rightarrow c\bar{c}, H \rightarrow gg$ ), the inference performance on Herwig7 samples shows a convergent trend relative to the Pythia8 baseline. As the training dataset expands toward  $10^6$  events, the measurement uncertainties derived from Herwig7 (blue lines) asymptotically approach or maintain a stable offset from the Pythia8 results (green lines). This suggests that for flavor tagging and gluon identification, increasing the training statistics allows the network to extract robust features that are consistent across the Cluster and String fragmentation models.

In contrast, the four-body vector boson processes ( $H \rightarrow WW^*, H \rightarrow ZZ^*$ ) exhibit a divergent trend. At low statistics ( $10^3$  events), the performance gap between the two generators is minimal. However, as the statistics increase, the gap widens significantly: while the performance on the Pythia8 test set improves rapidly with a steep slope, the improvement on the Herwig7 samples is more modest. As illustrated by the red curves representing the relative difference, the discrepancy increases with the training set size for these channels. This divergence indicates that for complex four-jet topologies, the network learns high-order kinematic correlations specific to the training generator (Pythia8) that do not fully generalize to the Herwig7 environment. Consequently, measurements of  $H \rightarrow WW^*/ZZ^*$  will be subject to larger modeling systematic uncertainties compared to the two-body decay modes.

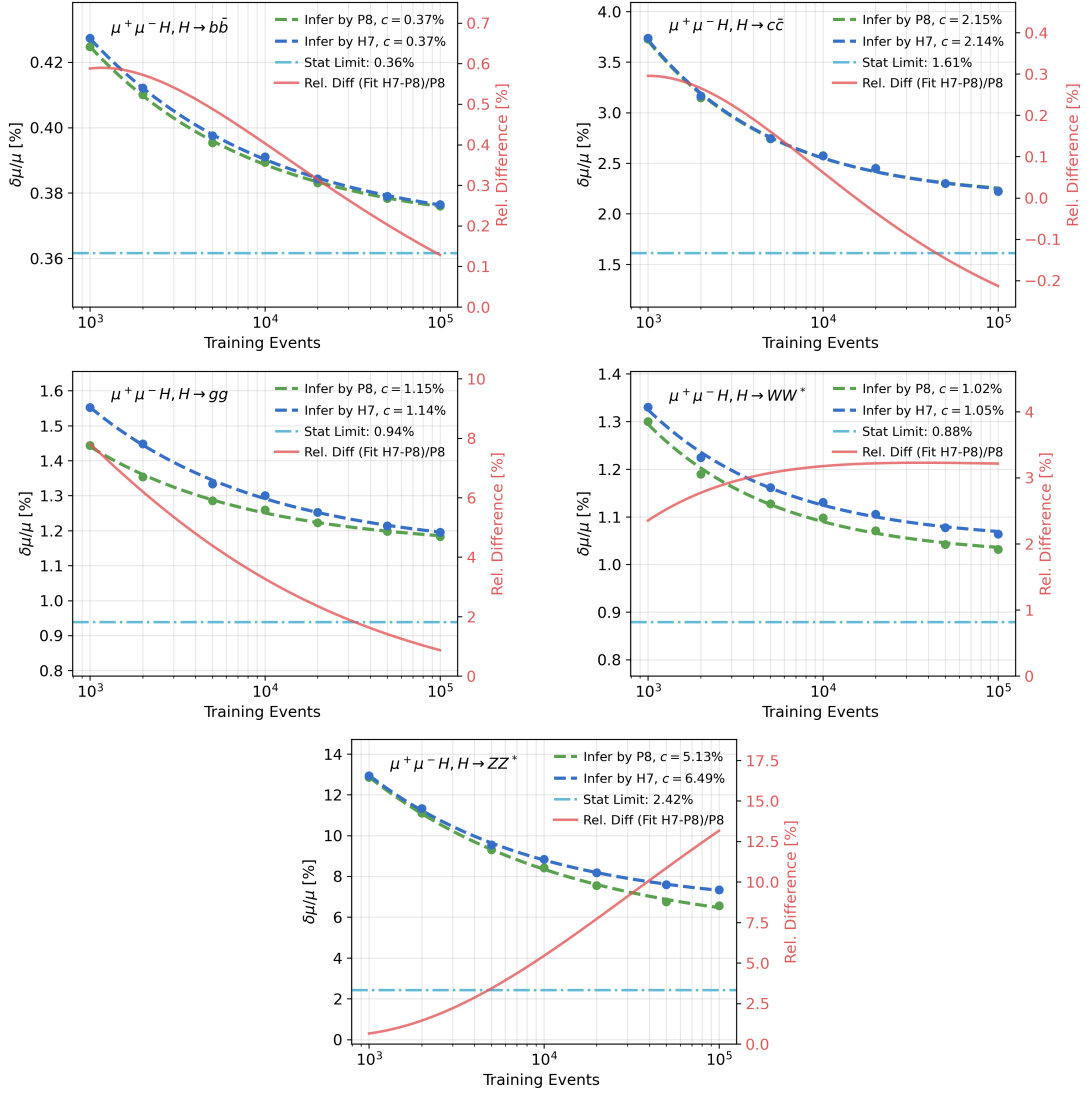


**Figure 10.** Scaling of measurement statistical uncertainty with training dataset size for the  $Z(\mu^+ \mu^-)H$  channel, comparing results with Herwig7 and Pythia8 inference.

## 5 Discussion and Summary

This paper reports a systematic evaluation of Higgs boson hadronic decay branching ratio measurements at future  $e^+e^-$  Higgs factories, utilizing a holistic approach based on the ParticleNet architecture. By processing each collision event as a comprehensive particle cloud, this method preserves the full constituent-level information, allowing the model to leverage global kinematic correlations characteristic of the  $ZH$  process. The analysis was performed based on the CEPC 240 GeV run with an integrated luminosity of  $20 ab^{-1}$ .

Our results demonstrate that the holistic approach yields significant precision improvements over traditional methods. In the  $Z(\mu^+ \mu^-)H$  channel, the relative statistical uncertainties are projected to be 0.38% ( $b\bar{b}$ ), 2.23% ( $c\bar{c}$ ), 1.18% ( $gg$ ), 1.03% ( $WW^*$ ), and

6.56% ( $ZZ^*$ ). In the  $Z(\nu\bar{\nu})H$  channel, with a physics-driven kinematic pre-selection, the relative statistical uncertainties are projected to be 0.17% ( $b\bar{b}$ ), 0.86% ( $c\bar{c}$ ), 0.47% ( $gg$ ), 0.43% ( $WW^*$ ), and 2.55% ( $ZZ^*$ ). A global combination of these channels, along with projections for the  $Z(e^+e^-)H$ ,  $Z(\tau^+\tau^-)H$ , and  $Z(q\bar{q})H$  channels, confirms that the holistic approach enables measurement precision reaching 0.11% for  $H \rightarrow b\bar{b}$  and 0.56% for the challenging  $H \rightarrow c\bar{c}$  channel.

We observe a significant scaling behavior with the holistic approach, where the identification power and anticipated accuracy scale with the increase in training data size. We observe that the accuracies asymptotically saturate towards a limit, which closely approaches the ultimate statistical limits for the  $H \rightarrow b\bar{b}$ ,  $H \rightarrow c\bar{c}$ , and  $H \rightarrow gg$  measurements. Furthermore, our analysis suggests that combining a physics-driven pre-selection with the holistic approach significantly enhances performance and accelerates convergence.

To quantify the theoretical uncertainties relevant to different hadronization models, we analyze the scaling behavior using different combinations of training and inference datasets. Interestingly, we observe distinct behaviors: for the  $b\bar{b}$ ,  $c\bar{c}$ ,  $gg$  processes, the difference in anticipated accuracies diminishes or remains stable as statistics increase, while the  $WW^*$ ,  $ZZ^*$  processes show greater sensitivity to the generator model. Nevertheless, the smooth scaling behavior observed across all channels suggests that these uncertainties are robust and controllable.

In summary, the holistic approach offers a promising avenue for precision Higgs physics at future Higgs factories. While rigorous control of systematic uncertainties remains a prerequisite for the final experimental precision, the potential of this methodology extends well beyond the standard Higgs decay modes. By fully exploiting the constituent-level information and global kinematic correlations of the collision events, this approach can be generalized to a broad spectrum of physics scenarios, including the search for rare decays and subtle Beyond the Standard Model (BSM) signatures. Ultimately, the holistic approach serves as a critical tool to maximize the physics reach and discovery potential of future Higgs factories.

## 6 Acknowledgements

This work was supported by the National Key R&D Program of China (Grant Nos. 2024YFA1610603) and NSFC funded International Collaboration Fund for Research teams W2441004.

## References

- [1] ATLAS collaboration, *Observation of a new particle in the search for the Standard Model Higgs boson with the ATLAS detector at the LHC*, *Phys. Lett. B* **716** (2012) 1 [[1207.7214](https://arxiv.org/abs/1207.7214)].
- [2] CMS collaboration, *Observation of a New Boson at a Mass of 125 GeV with the CMS Experiment at the LHC*, *Phys. Lett. B* **716** (2012) 30 [[1207.7235](https://arxiv.org/abs/1207.7235)].
- [3] The European Strategy Group, *Deliberation document on the 2020 Update of the European Strategy for Particle Physics*, Tech. Rep. [CERN-ESU-014](https://cds.cern.ch/record/2603271), Geneva (2020), [DOI](https://doi.org/10.23737/cern-2020-014).

- [4] J. de Blas et al., *Physics Briefing Book: Input for the 2026 update of the European Strategy for Particle Physics*, [2511.03883](#).
- [5] CEPC STUDY GROUP collaboration, *CEPC Conceptual Design Report: Volume 1 - Accelerator*, [1809.00285](#).
- [6] CEPC STUDY GROUP collaboration, *CEPC Conceptual Design Report: Volume 2 - Physics & Detector*, [1811.10545](#).
- [7] CEPC STUDY GROUP collaboration, *CEPC Technical Design Report: Accelerator, Radiat. Detect. Technol. Methods* **8** (2024) 1 [[2312.14363](#)].
- [8] CEPC STUDY GROUP collaboration, *CEPC Technical Design Report - Reference Detector*, [2510.05260](#).
- [9] I. Agapov et al., *Future Circular Lepton Collider FCC-ee: Overview and Status*, in *Snowmass 2021*, 3, 2022 [[2203.08310](#)].
- [10] ILC collaboration, H. Baer et al., eds., *The International Linear Collider Technical Design Report - Volume 2: Physics*, [1306.6352](#).
- [11] L. Linssen, A. Miyamoto, M. Stanitzki and H. Weerts, *Physics and detectors at clic: Clic conceptual design report*, 2012.
- [12] H. Liang, Y. Zhu, Y. Wang, Y. Che, C. Zhou, H. Qu et al., *Jet-Origin Identification and Its Application at an Electron-Positron Higgs Factory*, *Phys. Rev. Lett.* **132** (2024) 221802 [[2310.03440](#)].
- [13] Y. Wang, H. Liang, Y. Zhu, Y. Che, X. Xia, H. Qu et al., *One-to-one correspondence reconstruction at the electron-positron Higgs factory*, *Comput. Phys. Commun.* **314** (2025) 109661 [[2411.06939](#)].
- [14] Y. Zhu, H. Liang, Y. Wang, Y. Che, H. Wang, C. Zhou et al., *Holistic approach and Advanced Color Singlet Identification for physics measurements at high energy frontier*, [2506.11783](#).
- [15] CEPC PHYSICS STUDY GROUP collaboration, *The Physics potential of the CEPC. Prepared for the US Snowmass Community Planning Exercise (Snowmass 2021)*, in *Snowmass 2021*, 5, 2022 [[2205.08553](#)].
- [16] J. Alwall, R. Frederix, S. Frixione, V. Hirschi, F. Maltoni, O. Mattelaer et al., *The automated computation of tree-level and next-to-leading order differential cross sections, and their matching to parton shower simulations*, *JHEP* **07** (2014) 079 [[1405.0301](#)].
- [17] C. Bierlich et al., *A comprehensive guide to the physics and usage of PYTHIA 8.3*, *SciPost Phys. Codeb.* **2022** (2022) 8 [[2203.11601](#)].
- [18] DELPHES 3 collaboration, *DELPHES 3, A modular framework for fast simulation of a generic collider experiment*, *JHEP* **02** (2014) 057 [[1307.6346](#)].
- [19] H. Qu and L. Gouskos, *ParticleNet: Jet Tagging via Particle Clouds*, *Phys. Rev. D* **101** (2020) 056019 [[1902.08570](#)].
- [20] X. Ma, Z. Wu, J. Wu, Y. Huang, G. Li, M. Ruan et al., *Measurements of decay branching fractions of the Higgs boson to hadronic final states at the CEPC\**, *Chin. Phys. C* **49** (2025) 053001 [[2410.04465](#)].
- [21] X. Wang, Y. Zhu, C. Zhu, J. Jiang, M. Ruan, K. Wang et al., *Deep-learning jet flavor tagging for precision hadronic Higgs measurements at future  $e^+e^-$  Higgs factories*, [2512.21558](#).

- [22] A. Del Vecchio, J. Eysermans, L. Gouskos, G. Iakovidis, A. Maloizel, G. Marchiori et al., *Precision Measurements of Higgs Hadronic Decay Modes at the FCC-ee*, [2511.23149](https://arxiv.org/abs/2511.23149).
- [23] Y. Zhu, H. Cui and M. Ruan, *The Higgs $\rightarrow b\bar{b}, c\bar{c}, gg$  measurement at CEPC*, *JHEP* **11** (2022) 100 [[2203.01469](https://arxiv.org/abs/2203.01469)].
- [24] G. Bewick et al., *Herwig 7.3 release note*, *Eur. Phys. J. C* **84** (2024) 1053 [[2312.05175](https://arxiv.org/abs/2312.05175)].
- [25] B.R. Webber, *A QCD Model for Jet Fragmentation Including Soft Gluon Interference*, *Nucl. Phys. B* **238** (1984) 492.
- [26] T. Sjostrand, *The Lund Monte Carlo for Jet Fragmentation*, *Comput. Phys. Commun.* **27** (1982) 243.
- [27] B. Andersson, *The Lund Model*, vol. 7, Cambridge University Press (1998), [10.1017/9781009401296](https://doi.org/10.1017/9781009401296).